Remote Sensing of Environment xxx (2015) xxx–xxx

Contents lists available at ScienceDirect

Remote Sensing of Environment

journal homepage: www.elsevier.com/locate/rse

Specifying the saturation temperature for the HyspIRI 4-μm channel

V.J. Realmuto [a,*], P.E. Dennison [b], M. Foote [a], M.S. Ramsey [c], M.J. Wooster [d], R. Wright [e]

[a] Jet Propulsion Laboratory, California Institute of Technology, Pasadena, CA, USA
[b] University of Utah, Salt Lake City, UT, USA
[c] University of Pittsburgh, Pittsburgh, PA, USA
[d] King's College London, London, UK
[e] University of Hawaii at Manoa, Honolulu, HI, USA

ARTICLE INFO

Article history:
Received 30 June 2014
Received in revised form 18 April 2015
Accepted 24 April 2015
Available online xxxx

Keywords:
HyspIRI
Wildland fires
Volcanoes
Mid-infrared remote sensing

ABSTRACT

The investigation of high-temperature natural phenomena, such as wildland fires and active lava flows, is a primary science objective for the proposed Hyperspectral Infrared Imager (HyspIRI) mission. Current planning for HyspIRI includes a mid-infrared (MIR) channel centered at 4 μm that will allow measurement of radiance emitted from high-temperature targets. In this paper we present the results of a study to specify the saturation temperature for the MIR channel. This study was based on reviews of the literature, together with case studies of airborne and satellite-based data acquired over high-temperature targets. The spatial resolution of MIR radiance measurements is an important consideration in the remote sensing of high-temperature phenomena, due to the presence of materials at different temperatures within the area covered by an image pixel. The HyspIRI MIR channel will provide a spatial resolution of 60 m, which is ~40 times finer (in terms of area) than the finest spatial resolution provided by heritage instruments (370 m). This fine spatial resolution will increase the probability that high-temperature targets fill an image pixel and, therefore, the HyspIRI MIR channel will require a saturation temperature 2 to 4 times higher than the saturation limits of heritage instruments. Based on our study, we recommend a saturation temperature of 1200 K (927 °C). This recommendation accounts for the high temperatures expected for natural phenomena, expected performance of the MIR channel, and overlap in sensitivity between the MIR and thermal infrared (7.5–12 μm) HyspIRI channels.

1. Introduction

Temperature is a critical variable for understanding wildfire and lava flows. Satellite-based remote sensing provides a safe and practical means for estimating the temperatures of fires and lava flows, provided that the sensor is not overwhelmed by the high levels of radiance emitted by these targets. Fire temperature is an important control on the emission of carbon monoxide, carbon dioxide, and aerosols (Andreae & Merlet, 2001; Pereira et al., 2009), as the efficiency of fuel combustion increases with an increase in the temperature of a fire. The temperature, duration, and intensity of fires have important impacts on soil chemistry and hydrology, seed dormancy, and vegetation recovery following fire (e.g., Bradstock & Auld, 1995; Brooks, 2002; DeBano, 2000; Drewa, Platt, & Moser, 2002; Odion & Davis, 2000). The rate at which lava flows cool, together with the effusion rate of lava, controls the final dimensions and morphology of flows (e.g., Crisp & Baloga, 1990a,b; Pieri & Baloga, 1986). As reviewed by Harris, Dehn, & Calvari (2007) and Harris and Baloga (2009), a variety of methods have been developed to infer lava effusion rates from measurements of the surface temperatures of active flows and domes. Temperature measurements are also used to predict the behavior of active lava flows (e.g. Rowland, Garbeil, & Harris, 2005; Wright, Garbeil, & Harris, 2008) and detect changes in the flux of radiant energy from summit craters that can signal impending eruptions or changes in the behavior of on-going eruptions (e.g. Glaze, Francis, & Rothery, 1989; Kaneko, Wooster, & Nakada, 2002; Wooster & Rothery, 1997).

The HyspIRI mission (see Table 1 for a list of acronyms), as defined by a recent review of the NASA and NOAA earth-observation programs (National Research Council, 2007), will provide VSWIR imaging spectroscopy and TIR multispectral imaging at a spatial resolution of 60 m. The TIR imager will include a MIR channel, centered at 4 μm, designed for the observation of high-temperature phenomena. In this paper we present the results of our study to define a saturation temperature, or threshold, for the HyspIRI MIR channel. The study was based on a review of literature discussing the remote sensing of high-temperature phenomena together with case studies based on the best-available

* Corresponding author at: M.S 183-501, Jet Propulsion Laboratory, 4800 Oak Grove Drive, Pasadena, CA 91109, USA. Tel.: +1 818 354 1824.
E-mail address: vincent.j.realmuto@jpl.nasa.gov (V.J. Realmuto).

http://dx.doi.org/10.1016/j.rse.2015.04.028
0034-4257/

Table 1
List of acronyms.

AASTR	Advanced Along-Track Scanning Radiometer
ASTER	Advanced Spaceborne Emission and Reflection Radiometer
ATSR	Along-Track Scanning Radiometer
AVHRR	Advanced Very High Resolution Radiometer
AVIRIS	Airborne Visible/Infrared Imaging Spectrometer
BIRD	Bi-spectral Infrared Detection (Mission)
DAIS	Digital Airborne Imaging Spectrometer
FLIR	Forward-Looking Infrared (Camera)
GOES	Geostationary Operational Environmental Satellite
HSRS	Hot Spot Recognition System
HyspIRI	Hyperspectral and Infrared Imager
IFOV	Instantaneous Field-of-View
Landsat TM	Landsat Thematic Mapper
MASTER	MODIS/ASTER Airborne Simulator
MESMA	Multiple Endmember Spectral Mixture Analysis
MIR	Mid-Infrared
MIVIS	Multispectral Infrared and Visible Imaging Spectrometer
MMCM	Minimized Multi-Component Model(ing)
MODIS	Moderate-Resolution Imaging Spectroradiometer
MSG	Meteosat Second Generation
NASA	National Aeronautics and Space Administration
NEΔT	Noise-Equivalent Change (Delta) in Temperature
NPP	National Polar-Orbiting Partnership
NOAA	National Oceanic and Atmospheric Administration
NRC	National Research Council
SEVIRI	Spinning-Enhanced Visible-Infrared Imager
TDI	Time-Delayed Integration
TIR	Thermal Infrared
TRMM	Tropical Rainfall Measuring Mission
USGS	United States Geological Survey
VIIRS	Visible Infrared Imaging Radiometer Suite
VIRS	Visible and Infrared Scanner
VSWIR/V-SWIR	Visible and Shortwave Infrared

radiance data measured at spatial resolutions finer than 60 m. We find that a saturation temperature of 1200 K (927 °C) should allow imaging of high-temperature targets with low probability of saturation.

2. HyspIRI heritage and anticipated performance

Table 2 lists current and recent satellite instruments equipped with MIR channels positioned near 4 μm. The MIR has proven to be an essential spectral region for remote measurement of high-temperature phenomena, and the data from all these instruments have been applied to fire- and eruption-detection algorithms (e.g. Briess et al., 2003; Csiszar & Sullivan, 2002; Csiszar, Morisette, & Giglio, 2006; Gao, Xiong, Li, & Wang, 2007; Giglio, Kendall, & Justice, 1999; Giglio, Kendall, & Tucker, 2000, and Giglio, Kendall, & Mack, 2003; Harris & Thornber, 1999 and Harris et al., 2001; Justice et al., 2002; Kaufman et al., 2003; Roberts et al., 2005; Wright, Flynn, Garbeil, Harris, & Pilger, 2002, 2004; and Xu, Wooster, Roberts, & Freeborn, 2010). The latest instrument, VIIRS, was launched aboard the Suomi NPP platform in October 2011, and VIIRS-based fire products are still under evaluation (Csiszar et al., 2014; Schroeder, Oliva, Giglio, & Csiszar, 2014).

Most previous satellite instruments with MIR channels have had saturation thresholds between 311 K and 367 K (Table 2), maximizing sensitivity to radiance emitted at ambient background temperatures but readily saturating over high-temperature targets. Channels specifically designed for measuring radiance from high-temperature targets, such as BIRD HSRS, MODIS Channel 21, and VIIRS Channel M13, have higher saturation temperatures.

The 60-m spatial resolution of HyspIRI MIR represents a significant improvement over that of the heritage instruments (Table 2) and, accordingly, the recommended saturation temperature for HyspIRI is 2 to 4 times higher than those of the heritage instruments. To illustrate the impact of spatial resolution on saturation temperature, consider an isolated high-temperature feature, or component, within the IFOV of a sensor. A reduction in the size of the IFOV (i.e., improvement in spatial resolution) will increase the fraction of the IFOV occupied by the high-temperature component and increase the measured radiance. As we show in Fig. 1, radiance is a non-linear function of temperature and, therefore, the measured radiance will increase exponentially as the fraction of the high-temperature component within the IFOV increases.

The anticipated performance of the HyspIRI MIR channel is characterized by Figs. 1 and 2. Fig. 1 shows the spectral response of the MIR (4 μm) and TIR (8–12 μm) channels superimposed on the radiance spectra of blackbodies at temperatures of 300, 500, and 700 K. The blackbody spectra, calculated with the Planck Equation, illustrate that an increase in temperature results in non-linear increases in radiance, together with a shift in peak radiance to shorter wavelengths (Fig. 1). These phenomena allow us to detect and isolate the contributions of high-temperature components to the radiance measured within an IFOV and, ultimately, estimate the temperatures of these components.

The HyspIRI TIR channels are well-positioned to measure the radiance of a blackbody at 300 K, the approximate average temperature of the Earth's surface. The radiance of the 700 K blackbody peaks near the center of the proposed MIR channel. The TIR channels are designed to saturate at temperatures near 500 K, the approximate cross-over temperature at which the blackbody radiance at 4 and 8 μm is roughly equivalent (Fig. 1).

Fig. 2 shows the simulated sensitivity of the HyspIRI MIR channel as a function of saturation and scene temperatures. The metric for sensitivity is the NEΔT, which is the smallest difference in temperature that can be measured in the presence of noise. In general, sensitivity in the MIR improves (i.e., NEΔT decreases) with increasing scene temperature. The choice of saturation temperature has the greatest impact on sensitivity to scene temperatures < 400 K. In this temperature regime the sensitivity decreases (i.e., NEΔT increases) with an increase in the saturation temperature. At the recommended saturation threshold of 1200 K, NEΔT will range between 7.5 and 4.5 K for scene temperatures between 320 and 340 K (Fig. 2).

The potential impact of HyspIRI's high spatial resolution to fire detection programs is illustrated in Fig. 3, which is a plot of the theoretical limit, or threshold, of detection for the MODIS fire algorithm as a function of the size and temperature of a fire (Csiszar et al., 2006; Giglio, Descloitres, Justice, & Kaufman, 2003). For MODIS, fires with areas of 100 and 10,000 m^2 would require temperatures of at least 1200 and 500 K, respectively, to be detected. The temperatures 1200 and 500 K

Table 2
Heritage instruments for the HyspIRI MIR channel.

Instrument	Central wavelength (μm)	Spatial resolution (at nadir)	Temporal coverage (daytime)	Saturation temperature
ATSR/AATSR	3.7	1 km/1.5 × 2 km	3 day revisit	311 K (38 °C)
AVHRR	3.7	1.1 km	Daily (NOAA 18 + 19)	~321.5 K (48.4 °C)
GOES Imager	3.9	2.3 × 4 km	3 h/15–30 min	335 K (62 °C)
HSRS	3.8	0.370 km	Targeted	600 K (327 °C)
MODIS	3.95	1 km	Daily (Terra + Aqua)	Ch. 21: 478/506 K (205/233 °C) Ch. 22: 330 K (57 °C)
SEVIRI	3.9	3 km	15 min	335 K (62 °C)
VIIRS-M13	4.0	0.750 km	Daily	634 K (361 °C)
VIIRS-I4	3.74	0.375 km	Daily	367 K (94 °C)
VIRS	3.75	2.4 km	2 day revisit	321 K (48 °C)

Please cite this article as: Realmuto, V.J., et al., Specifying the saturation temperature for the HyspIRI 4-μm channel, *Remote Sensing of Environment* (2015), http://dx.doi.org/10.1016/j.rse.2015.04.028

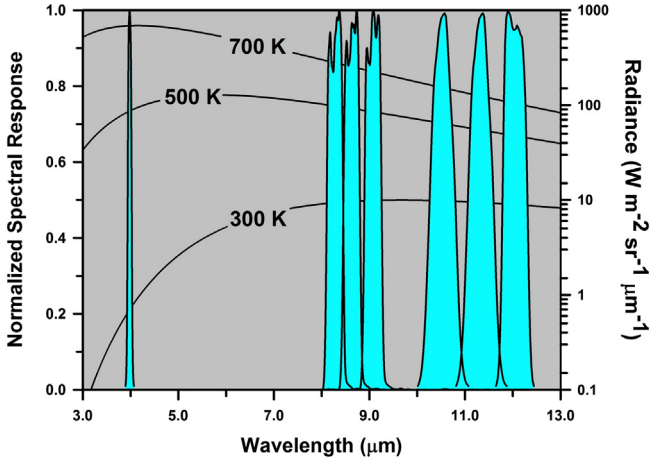

Fig. 1. Normalized spectral response of proposed HyspIRI-TIR channels. The spectral response functions, shown in blue, are superimposed on blackbody radiance spectra for temperatures of 300, 500, and 700 K (27, 227, and 427 °C). Note that the blackbody radiance at 4.0 and 8.5 μm is roughly equivalent for a temperature of 500 K. (For interpretation of the references to color in this figure legend, the reader is referred to the web version of this article.)

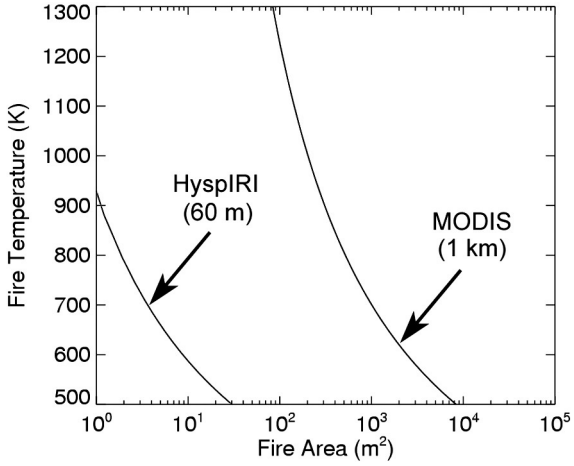

Fig. 3. Detection thresholds for the MODIS fire detection algorithm at the spatial resolutions of MODIS and HyspIRI. Detection threshold is a function of fire temperature vs. area (L. Giglio, pers. communication).

represent the upper and lower thresholds for flaming and smoldering combustion, respectively, in the MODIS fire algorithm (e.g., Kaufman, Kleidman, & King, 1998). HyspIRI will be sensitive to fires at lower temperatures or smaller areas, relative to MODIS. For a fire at 500 K, the necessary area threshold drops from 10,000 m^2 (MODIS) to 30 m^2 (HyspIRI).

3. Literature review

3.1. Temperature estimation techniques

To estimate the temperature of hot targets within a sensor's IFOV, Dozier (1981) and Matson and Dozier (1981) modeled the radiance measured in a spectral channel as the linear combination of the radiance emitted from two temperature components. One component represented the high-temperature target (T_h), while the other represented the background temperature (T_b). This model was originally developed for the AVHRR instrument, utilizing the radiance measured in Channels 3 (3.55–3.93 μm) and 4 (10.5–11.5 μm). Denoting the radiance at 4 and 11 μm as L_4 and L_{11}, respectively, the relative contributions of the high-temperature and background components to the radiance were modeled as:

$$L_4 = pB_4(T_h) + (1-p)B_4(T_b), \text{ and}$$
$$L_{11} = pB_{11}(T_h) + (1-p)B_{11}(T_b), \quad (1)$$

where p is the size fraction, relative to the image pixel, occupied by the high-temperature component, and B_4 and B_{11} represent the blackbody radiance at 4 and 11 μm, respectively. In most applications T_b is estimated from pixels surrounding the pixel of interest. Two-component radiance models have been applied to numerous studies of wildfires, coal fires, and volcanic phenomena, incorporating data from ASTER (Eckmann, Roberts, & Still, 2009; Giglio et al., 2008), AVHRR (e.g., Giglio et al., 1999; Harris, Blake, Rothery, & Stevens, 1997; Harris, Vaughan, & Rothery, 1995; Langaas, 1993), Landsat TM (e.g., Glaze et al., 1989; Oppenheimer, Francis, Rothery, & Carlton, 1993, Prakash & Gupta, 1999; Rothery, Francis, & Wood, 1988; Wooster & Kaneko, 2001; Wright, Flynn, & Harris, 2001), ATSR (Rothery, Coltelli, Pirie, Wooster, & Wright, 2001; Wooster & Rothery, 1997), and BIRD (Oertel, Zhulov, Thamm, Roehrig, & Orthmann, 2004; Siegert et al., 2004; Wooster, Zhukov, & Oertel, 2003), as well as airborne instruments such as AVIRIS (Oppenheimer, Rothery, Pieri, Abrams, & Carrere, 1993), DAIS (Lombardo, Buongiorno, & Amici, 2006 and Lombardo, Merucci, & Buongiorno, 2006), and MIVIS (Lombardo & Buongiornio, 2006; Lombardo, Harris, Calvari, & Buongiornio, 2009). Lombardo, Merucci, et al. (2006) and Vaughan et al. (2010) present comprehensive evaluations of the application of two-component models to airborne (DAIS) and satellite (ASTER) data, respectively.

Most high-temperature phenomena involve more than two temperature components, and the application of two-component models to multi-component phenomena under-estimates the contributions of high-temperature components to the measured radiance. To address this shortcoming, Giglio and Kendall (2001) evaluated models with additional components representing smoldering fire, at a temperature intermediate to the flaming and background temperatures, and burned areas, at a temperature above the background temperature. Similarly, Harris et al. (1997) introduced an intermediate-temperature component, representing the hot crust formed at the surface of cooling lava flows, to an analysis of AVHRR data acquired during the 1991–1993 eruption of Mt. Etna. In both investigations, the additional model components provided insight into the radiative process but their contributions to the observed radiance were not constrained by these data.

Various investigators have explored the use of multiple spectral channels in to constrain multi-component models. Oppenheimer,

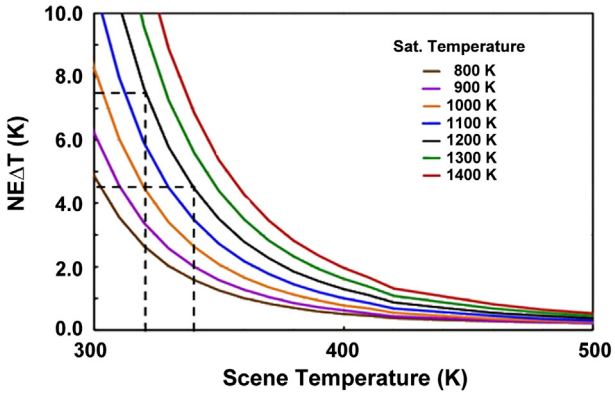

Fig. 2. Simulated sensitivity of the HyspIRI MIR (4-μm) channel to scene temperature. Sensitivity is expressed as NEΔT, or the smallest temperature change that can be detected in the presence of noise. Potential saturation temperatures are shown in the legend. For the recommended saturation temperature of 1200 K (927 °C), scene temperatures of 320 and 340 K (47 and 67 °C) result in an NEΔT of 7.5 and 4.5 K, respectively.

Rothery, et al. (1993) applied curve-fitting techniques to AVIRIS data to obtain estimates of the temperature and size of hot spots at Stromboli volcano. Harris, Flynn, Rothery, Oppenheimer, and Sherman (1999) applied a three-component model to triplets of Landsat TM channels to study the temperature structure of lava lakes. Wright and Flynn (2003) and Wright, Garbeil, and Davies (2010) present a non-linear minimization approach for estimating the temperature and relative size of multiple components from hyperspectral Hyperion data. As illustrated in Fig. 4, the Minimized Multi-Component Model (MMCM) treats the temperature and fractional area of each component as free parameters.

Multiple Endmember Spectral Mixture Analysis (MESMA), as described by Roberts et al. (1998), fits observed spectra with linear combinations, or mixtures, of endmember spectra selected from spectral libraries. The endmember spectra, and relative contribution of the spectra to the spectral mixture, are treated as free parameters. Dennison, Charoensiri, Roberts, Peterson, and Green (2006), Eckmann, Roberts, and Still (2008); Eckmann et al. (2009), Dennison and Matheson (2011), and Matheson and Dennison (2012) demonstrated that combinations of reflected and emitted radiance endmembers could be used to estimate fire temperatures and area from ASTER, AVIRIS, MASTER, and MODIS data. Emitted radiance endmembers for specific temperatures are typically calculated using radiative transfer modeling.

3.2. Published temperature estimates

Table 3 lists temperature estimates drawn from the literature, together with the estimates derived from our case studies (Section 4). We have organized the published temperatures into two categories defined by the spatial resolution of the corresponding radiance measurements. The published temperatures provide a useful perspective on the variability of high-temperature phenomena, but we had specific criteria for the consideration of published temperatures in our specification of saturation temperature. The shading in Table 3 indicates the temperatures estimate that met our criteria.

For the temperatures derived from radiance at spatial resolutions finer than 60 m (Table 3), we required that the radiance was aggregated to HyspIRI resolution (60 m) prior to the estimation of temperature. This stringent criterion eliminated all but one of the temperature estimates in this category, as such aggregation is unique to studies requiring the simulation of HyspIRI data. For the temperatures derived from radiance at spatial resolution coarser than 60 m, we required that the corresponding temperature components must fill at least one HyspIRI IFOV. This criterion was met by all but two of the published temperatures in this category.

The temperature estimates in our fine-scaled category were obtained with a variety of instruments and measurement techniques. For example, Wooster, Roberts, Perry, and Kaufman (2005) reported temperature estimates up to 1650 K for an experimental fire, based on measurements from a radiometer mounted on an 11.5-m observation tower. Riggan, Brass, and Lockwood (1993) and Riggan et al. (2004) described the use of an airborne IR scanner to measure temperatures in the range 1400–1600 K for leading edges of controlled burns in the Brazilian savanna. Dennison et al. (2006) estimated fire temperatures as high as 1500 K for the 2003 Simi Fire using AVIRIS data, with the majority of temperatures in the 750–950 K range. Eckmann et al. (2009) estimated fire temperatures up to 1500 K through an application of MESMA to ASTER SWIR data. Rose and Ramsey (2009) derived temperature estimates of ~1080 K from ASTER VNIR data acquired over open-channel lava flows from Klyuchevskoy Volcano. Prakash and Gupta (1999) and Wooster, Kaneko, Nakada, and Shimizu (2000) employed Landsat TM data to study coalfield fires (~1000 K), and an active lava dome at Unzen Volcano (~1100 K), respectively.

Matheson and Dennison (2012) evaluated the impact of spatial resolution on temperature estimates derived from AVIRIS data acquired over four wildfires in southern and central California (Fig. 5). The radiance data were resampled from their native resolution, which ranged from 5 to 20 m, to a range of resolutions up to 60 m. Using a MESMA-based technique, the mean temperature estimates derived from the 60-m data ranged between 663 and 804 K, decreasing an average of 30 K from the temperature estimates made at native resolution. The maximum temperatures of the four fires ranged from 960 to 1380 K, but the corresponding components were too small to fill the HyspIRI IFOV. The highest temperature with a component of sufficient size was 890 K.

The temperature estimates in our coarse-scaled category (Table 3) include the highest temperature encountered in our review. The VIIRS Nightfire system (Elvidge, Zhizhin, Hsu, & Baugh, 2013) detects 15,000 to 22,000 high-temperature features per day, based on night-time observations in the VSWIR and MIR. A statistical analysis of Nightfire results for a single day revealed a median temperature of 1750 K for features identified as gas flares. This temperature corresponds to a source area of ~0.3 m^2, based on theoretical detection limits (Elvidge et al., 2013), and we do not anticipate that gas flares will fill the HyspIRI IFOV.

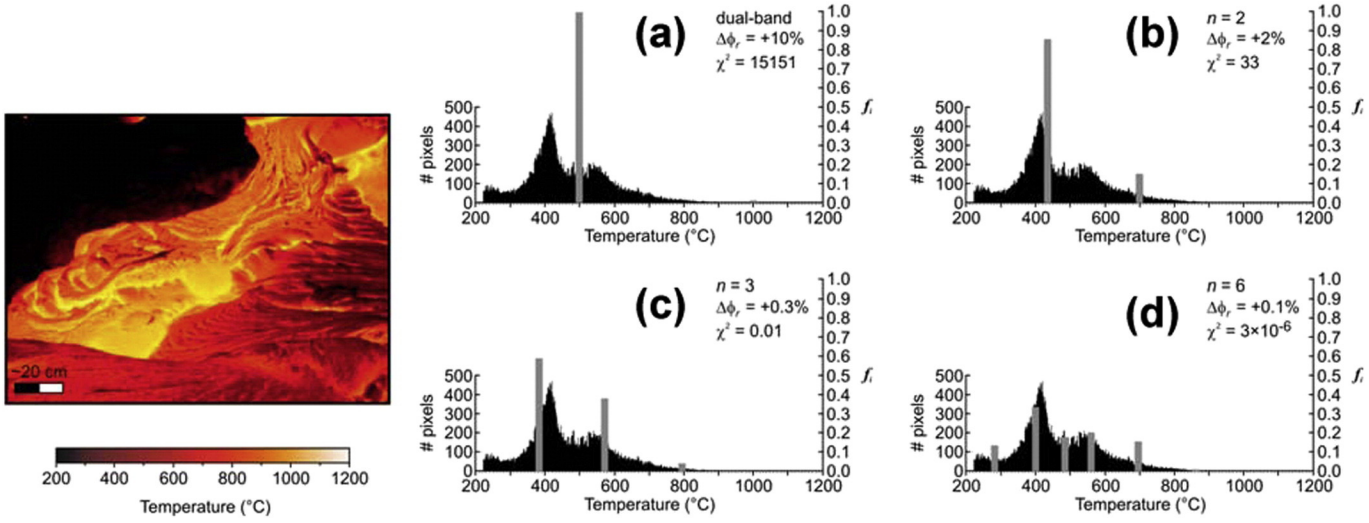

Fig. 4. Illustration of the Minimized Multi-Component Modeling (MMCM) technique (after Wright et al., 2010). The FLIR image (at left) represents the distribution of temperature components within a Hyperion pixel. The histograms (at right) show the model temperature components, area fractions of the components (gray bars), and Chi-Square (X^2) fit to the observed temperature distribution. (a) Temperature component derived with the conventional two-component (dual-band) model. (b–d) MMCM solutions with 2, 3, and 6 temperature components, respectively.

Please cite this article as: Realmuto, V.J., et al., Specifying the saturation temperature for the HyspIRI 4-μm channel, *Remote Sensing of Environment* (2015), http://dx.doi.org/10.1016/j.rse.2015.04.028

Table 3
Maximum temperatures from the literature review and case studies. Shading indicates the temperatures considered in our definition of the MIR saturation temperature. For spatial resolutions finer than 60 m, shading indicates that radiance was aggregated to 60 m spatial resolution prior to temperature estimation. For spatial resolutions coarser than 60 m, shading indicates that retrieved temperature corresponds to an area matching or exceeding the IFOV for a 60 m pixel.

Published study	Instrument	Maximum temperature
Spatial resolution < 60 m		
Wooster et al. (2005) (experimental burn)	Spectroradiometer	1650 K (1377 °C)
Dennison et al. (2006) (wildfire)	AVIRIS	1500 K (1277 °C)
Eckmann et al. (2009) (wildfire)	ASTER	1500 K (1277 °C)
Harris et al. (1999) (volcanic)	Landsat TM	1480 K (1207 °C)
Riggan et al. (1993); Riggan et al. (2004) (wildfire)	Airborne IR scanner	>1400 K (1127 °C)
Lombardo & Buongiornio (2006) (volcanic)	MIVIS	1400 K (1127 °C)
Wooster et al. (2000) (volcanic)	Landsat TM	1120 K (847 °C)
Rose & Ramsey (2009) (volcanic)	ASTER	1080 K (807 °C)
Prakash & Gupta (1999) (coal fire)	Landsat TM	1004 K (731 °C)
Matheson & Dennison (2012) (wildfire)	AVIRIS	890 K (617 °C)
Oppenheimer, Francis, et al. (1993), Oppenheimer, Rothery, et al. (1993) (volcanic)	AVIRIS	873 K (600 °C)
Spatial resolution > 60 m		
Elvidge et al. (2013) (gas flares)	VIIRS	1750 K (1477 °C)
Harris et al. (1995) (volcanic)	AVHRR	1325 K (1052 °C)
Harris et al. (1997) (volcanic)	AVHRR	1273 K (1000 °C)
Zhukov et al. (2003) (wildfire)	HSRS	1061 K (788 °C)
Siegert et al. (2004) (wildfire)	HSRS	860 K (587 °C)
Zhukov et al. (2006) (wildfire)	HSRS	860 K (587 °C)
Vaughan et al. (2008) (volcanic)	ASTER	810 K (537 °C)
Zhukov et al. (2006) (volcanic)	HSRS	540 K (267 °C)
Eckmann et al. (2008) (wildfire)	MODIS	500 K (227 °C)
Case study		
Sharpsand Creek Prescribed Burn, 2007	AGEMA Thermal Camera	1205/1260 K (932/987 °C)
Klyuchevskoy Volcano, 2007	ASTER	1043 K (770 °C)
Kilauea Volcano, 2007	ASTER	990 K (717 °C)
Nyamuragira Volcano, 2004	Hyperion	950 K (677 °C)
Poomacha Fire, 2007	AMS	795 K (522 °C)
Eyjafallajökull Volcano, 2010	Hyperion	750 K (477 °C)

Vaughan, Kervyn, Realmuto, Abrams, and Hook (2008) describe a rare application of two-component modeling to ASTER TIR imagery (90-m resolution), estimating temperatures up to ~820 K for carbonate-rich lava flows at Oldoinyo Lengai Volcano. The corresponding areas for the high-temperature components were too small to fill the HyspIRI IFOV. Turning to temperature estimates for components that would fill the HyspIRI IFOV, Harris et al. (1995) used AVHRR data to estimate that 240,000 m^2 of a lava flow erupted during the 1984 eruption of Krafla Volcano was at a temperature of ~1325 K. In an analysis of HSRS data acquired during an eruption of Mount Etna in 2002, Zhukov et al. (2005) found that 250,000 m^2 of an active lava flow was at a temperature of 540 K. Eckmann et al. (2008) applied MESMA to MODIS data acquired over wildland fires in the Ukraine and found high-temperature (500 K) components with areas up to 25,510 m^2. The area of these temperature components was validated through analyses of coincident ASTER SWIR data.

Temperature estimates derived from HSRS are prominent in our coarse-scaled category (Table 3). Of the heritage instruments listed in Table 2, the HSRS provided MIR radiance measurements with the finest spatial resolution (370 m) and highest saturation temperature (600 K). In addition, HSRS investigators incorporated two-component temperature modeling in their analyses. Table 4, a summary of analyses of HSRS data acquired over three wildfires and the 2002 eruption of Mount Etna, shows the variability in the temperature and size of high-temperature components within single events as well as between events. This variability led to our decision that the HyspIRI saturation temperature must exceed 1000 K.

4. Case studies

4.1. AMS survey of Southern California wildfires

In this section, we present an analysis of data acquired with the airborne Autonomous Modular Sensor (AMS), during the Southern California Firestorm of October 2007. The AMS flight campaigns are described by Ambrosia and Hinkley (2008). The configuration of AMS included spectral channels between 3.60 and 3.79 (Channel 11) and 10.26 and 11.26 μm (Channel 12). A total of 94 flight lines were collected over five fires: Grass Valley, Santiago, Poomacha, Witch, and Harris. The sensor was flown on the Ikhana unmanned platform, with altitudes ranging from approximately 7000 to 7500 m.

The first step in our analysis was to identify the flight lines that covered active fire fronts, with an emphasis on flight lines that were centered on fire fronts. This emphasis was necessitated by the difference between the total field-of-view of AMS (85°) and HyspIRI (51°). To approximate HyspIRI view zenith angles we restricted our analysis to AMS pixels within ±26° of nadir.

We projected the AMS data into UTM coordinates, based on the geolocation data for each pixel, and then aggregated the radiance data to the 60-m spatial resolution of HyspIRI. The map projection and aggregation operations were applied to floating point values to minimize the effects of re-sampling and interpolation on the simulated radiance. Finally, we converted the simulated HyspIRI radiance to brightness temperature through the inversion of the Planck Equation.

Our original plan for this case study was to use the AMS 3.7-μm radiance data to simulate the radiance that HyspIRI might encounter over a wildland fire. However, we could not follow this approach due to saturation of the 3.7-μm radiance data. As shown in Fig. 6, a scatterplot of brightness temperatures for the 3.7- and 10.5-μm channels (Channels 11 and 12, respectively), Channel 11 was saturated for temperatures greater than ~525 K. Due to this saturation we focused our analysis on Channel 12, which remained unsaturated for temperatures up to 650 K (Fig. 6). In addition, laboratory calibrations of Channel 12 indicated that this channel would not saturate for temperatures up to ~800 K (unpublished data courtesy of the Airborne Sensor Facility, NASA/Ames Research Center).

Fig. 7 is a demonstration of the aggregation of AMS data to the spatial resolutions of HyspIRI and MODIS. These AMS data were acquired over

Please cite this article as: Realmuto, V.J., et al., Specifying the saturation temperature for the HyspIRI 4-μm channel, *Remote Sensing of Environment* (2015), http://dx.doi.org/10.1016/j.rse.2015.04.028

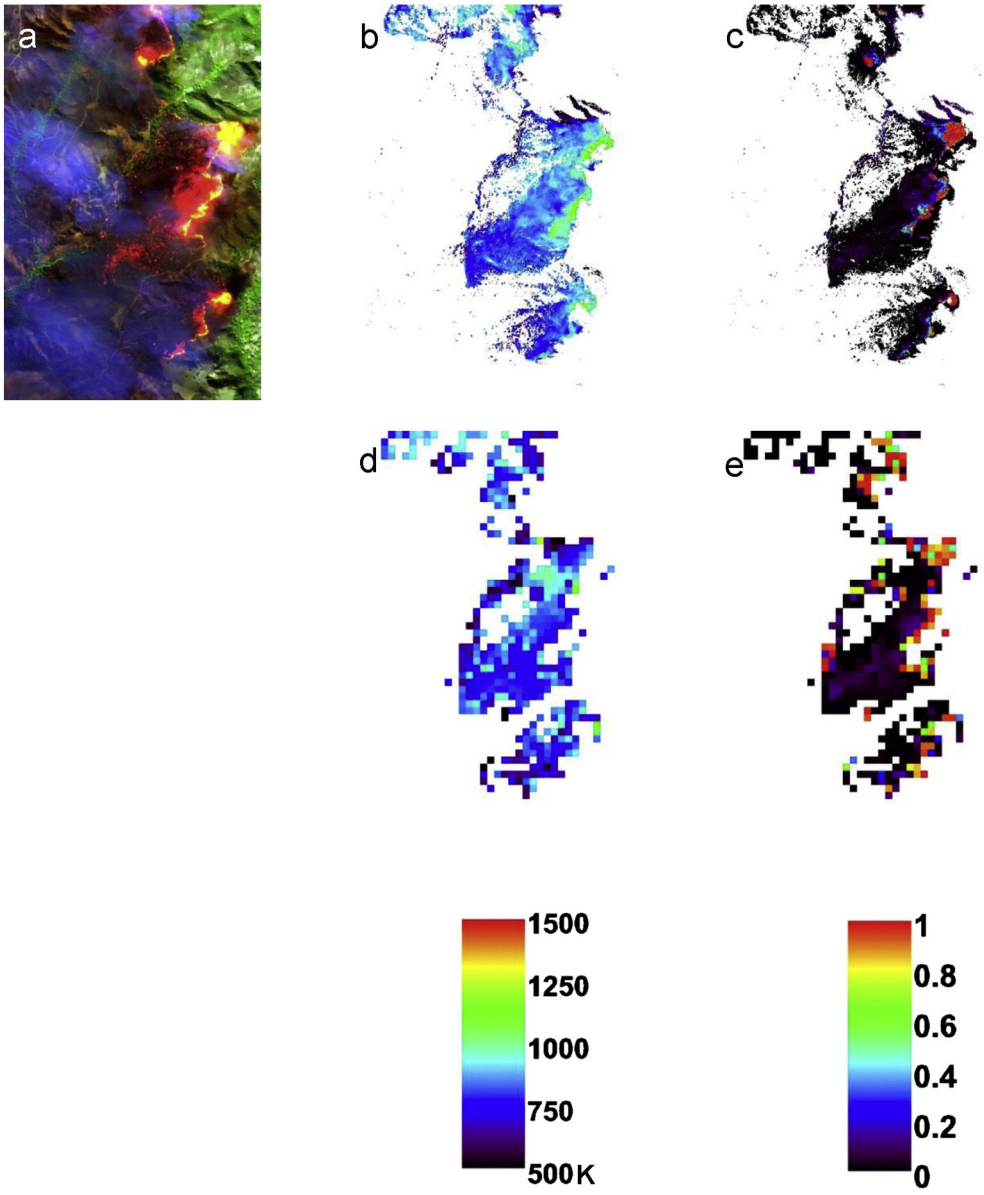

Fig. 5. Impact of spatial resolution on the temperature and area, relative to pixel dimensions, of temperature components generated with MESMA (after Matheson & Dennison, 2012). (a) Color-composite of AVIRIS radiance data acquired over the 2003 Simi Fire. (b and c) Temperature and fractional area, respectively, of temperature components derived from radiance at the native spatial resolution of 5 m. (d and e) Temperature and fractional area, respectively, of temperature components derived from radiance resampled to 60 m. The resampled temperature components with fractional areas approximately equal to 1 were eligible for the HyspIRI MIR saturation study.

Table 4
Temperature estimates derived from BIRD HSRS data via two-component modeling. T_f and A_f are the temperature and area of the high-temperature components, respectively.

Australia Fire[a] 2002-01-05		Kalimantan Fire[b] 2002-08-24/25		Lake Baikal Fire[c] 2003-06-16		Etna Lava Flow[d] 2002-11-02	
T_f	A_f (m^2)	T_f	A_f (m^2)	T_f	A_f (m^2)	T_f	A_f (m^2)
966 K (693 °C)	2000	860 K (587 °C)	25,000	851 K (578 °C)	63,000	540 K (267 °C)	250,000
803 K (530 °C)	9100	740 K (467 °C)	19,000	711 K (438 °C)	11,000	–	–
846 K (573 °C)	7000	650 K (377 °C)	46,000	775 K (502 °C)	21,000	–	–
908 K (635 °C)	6500	520 K (247 °C)	21,000	783 K (510 °C)	5300	–	–
1061 K (788 °C)	6400	720 K (447 °C)	11,000	850 K (577 °C)	4300	–	–
814 K (541 °C)	3300	690 K (417 °C)	30,000	860 K (587 °C)	19,000	–	–
–	–	590 K (317 °C)	33,000	763 K (490 °C)	7300	–	–
–	–	560 K (287 °C)	7000	–		–	–

[a] Zhukov et al. (2003).
[b] Siegert et al. (2004).
[c] Zhukov et al. (2006).
[d] Zhukov et al. (2005).

Please cite this article as: Realmuto, V.J., et al., Specifying the saturation temperature for the HyspIRI 4-μm channel, *Remote Sensing of Environment* (2015), http://dx.doi.org/10.1016/j.rse.2015.04.028

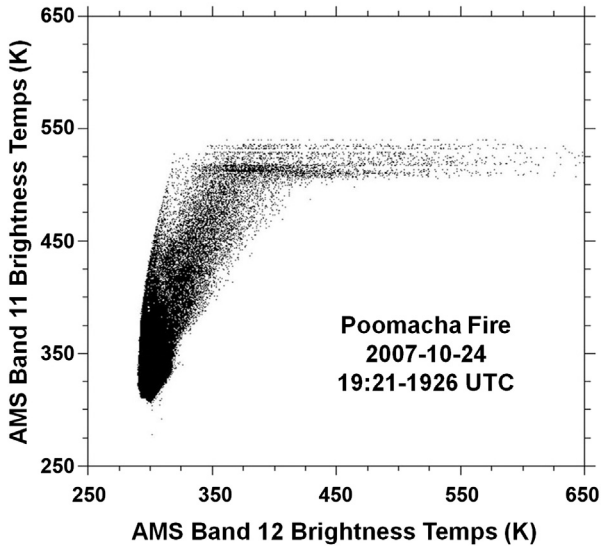

Fig. 6. Scatterplot of brightness temperatures from AMS Channels 11 (3.7 μm) and 12 (10.5 μm). Channel 11 was saturated for temperatures greater than 525 K (252 °C), while Channel 12 did not saturate for temperatures up to ~650 K (377 °C). Laboratory calibrations of AMS (unpublished data courtesy of Airborne Sensor Facility, NASA/Ames Research Center) indicated that Channel 12 could be used to measure temperatures up to ~800 K (527 °C).

the Santiago Fire on October 26, 2007. Fig. 7b is a map of Channel 11 brightness temperatures at the native spatial resolution of 8.3 m (following the re-projection to UTM coordinates). Fig. 7c and d show the results of aggregating the AMS data to the 60-m spatial resolution of HyspIRI and 1-km resolution of MODIS, respectively. The temperature estimates at HyspIRI resolution (Fig. 7c) are approximately 25 K lower than the estimates at native resolution (Fig. 7b), but the relative distribution, or pattern, of temperatures within the burn areas are preserved in the simulated HyspIRI scene. At the 1-km spatial resolution of MODIS (Fig. 7d), temperature estimates are 100 K lower than the estimates at native resolution (Fig. 7b), and information regarding the spatial distribution of temperature within the fire fronts has been lost.

A statistical analysis of the entire population of high-temperature pixels indicated that the Poomacha fire contributed approximately 60% of the pixels, and we considered the Poomacha data to be representative of the entire data set. We aggregated the Channel 12 radiance measurements from their native resolution to 60-m HyspIRI-scale pixels and calculated the brightness temperatures. The maximum temperature was 795 K, which is intermediate to the flaming and smoldering temperatures of 1000 and 600 K, respectively, defined originally by Kaufman, Justice, et al., 1998.

To evaluate the impact of sub-pixel temperature components on this maximum temperature estimate, we compared the cumulative histograms of the Poomacha temperatures at the native and aggregated resolutions (Fig. 8). The cumulative histograms diverge for temperatures higher than 380 K, which corresponds to a cumulative probability

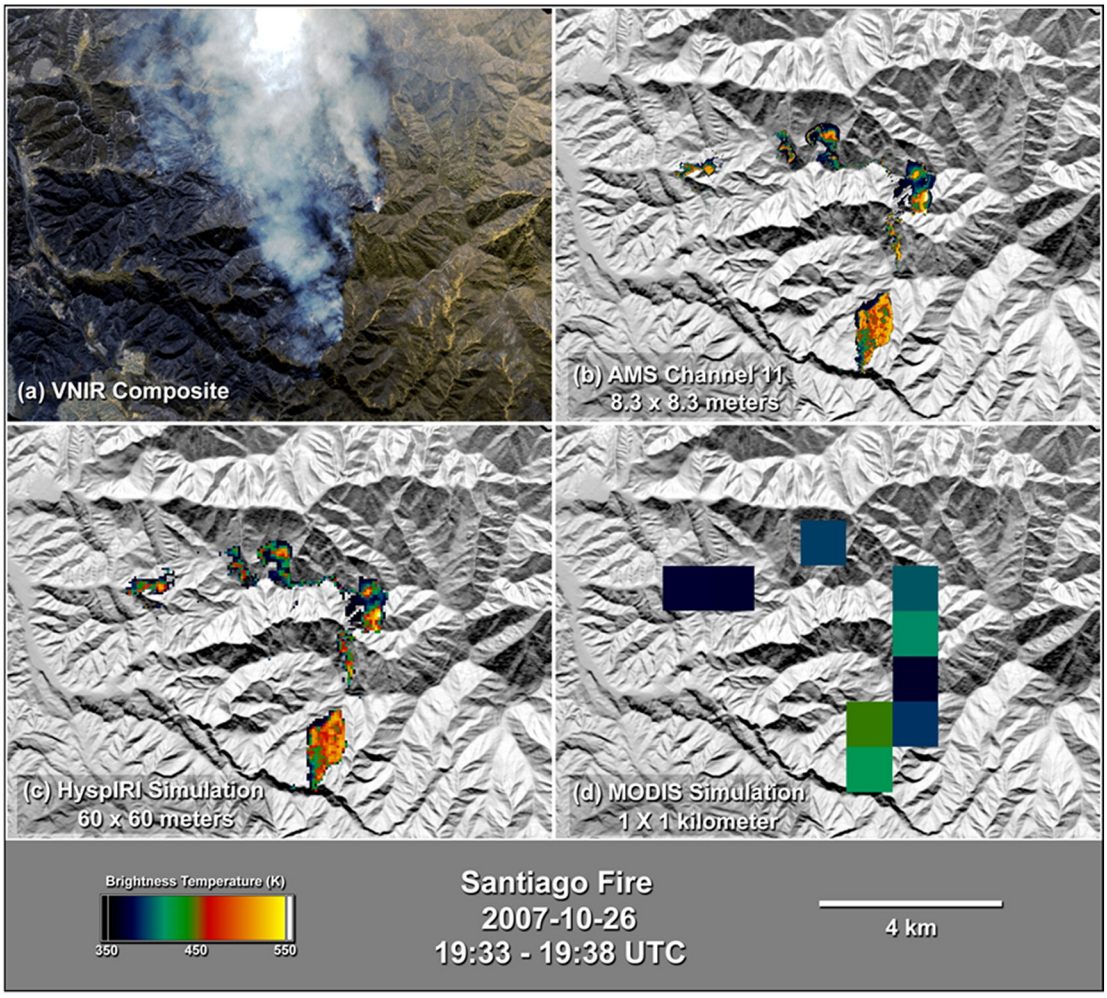

Fig. 7. Impact of spatial resolution on brightness temperature. (a) Color-composite of the AMS VNIR data. (b) Distribution of 4-μm temperatures at the native AMS resolution (8.3 m). (c) Distribution of temperatures following resampling to HyspIRI resolution (60 m). (d) Distribution of temperatures following resampling to MODIS resolution (1 km). The similarity between the temperature distributions at AMS (b) and HyspIRI (c) resolution suggests that the temperatures were uniform at scales up to 60 m.

Please cite this article as: Realmuto, V.J., et al., Specifying the saturation temperature for the HyspIRI 4-μm channel, *Remote Sensing of Environment* (2015), http://dx.doi.org/10.1016/j.rse.2015.04.028

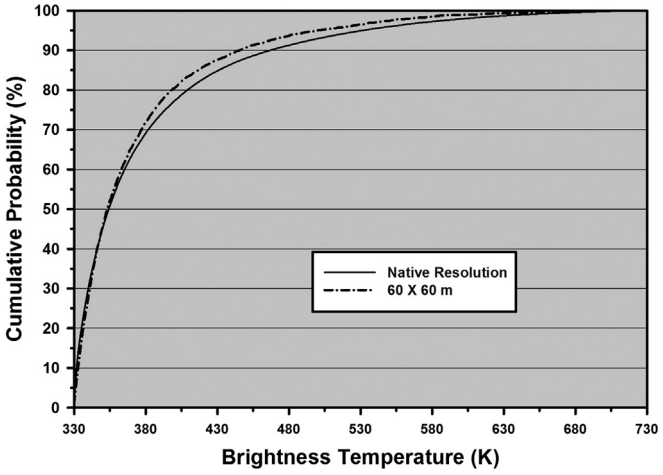

Fig. 8. Cumulative histograms of brightness temperatures at AMS (native) and HyspIRI (60 m) spatial resolutions. The divergence of the histograms for temperatures higher than 380 K (107 °C) is indicative of sub-pixel mixing.

of 60%. For cumulative probabilities higher than 60% the native temperatures are higher than the corresponding 60-m temperatures, although the separation between the histograms is generally less than 5%. This comparison indicates that the spatial distribution of the 60-m temperatures was similar to that of the native temperatures for the majority (60%) of the burn area, but sub-pixel mixing was a factor for apparent temperatures greater than 380 K. Therefore, we consider our maximum temperature of 795 K to be a lower bound on the HyspIRI MIR saturation temperature.

4.2. AGEMA camera data for Sharpsand Creek Fire

The Sharpsand Creek fire was a prescribed burn conducted via collaboration between the Canadian Forest Service, Ministry of Natural Resources, and scientists from King's College London, University of Edinburgh, and University of Leicester. Smith et al. (2010) describe the Sharpsand Creek site and the prescribed burn, which occurred on May 13, 2007. The burn site, located in northern Ontario, was a square plot of Jack Pine forest, measuring 10,000 m^2 (i.e., 1 ha).

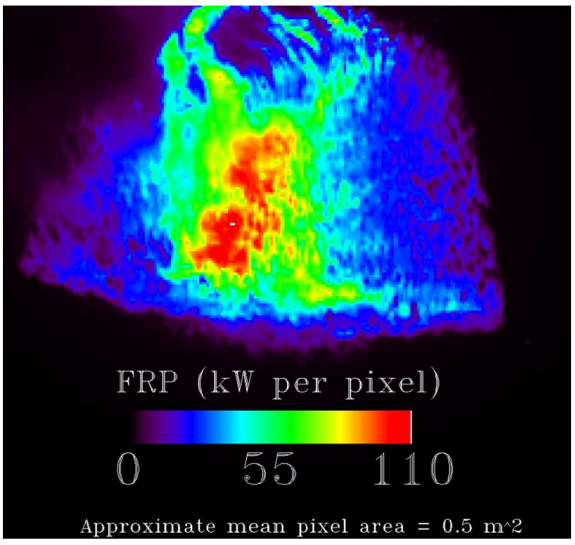

Fig. 9. Map of Fire Radiant Power (FRP) estimated for the Sharpsand Creek prescribed burn (Ontario, Canada). Temperature estimates of 1205 and 1260 K (932 and 987 °C) were obtained by aggregating the FRP and radiance, respectively, over a 60 × 60 m region of interest centered on the hottest portion of the fire.

The plot was lit with a perimeter ignition pattern, which resulted in flames reaching heights > 100 m. During the fire, a helicopter hovered above the plot, and IR imagery of the fire was collected using an AGEMA-550 thermal imaging camera equipped with a 3.9-μm narrow-band filter. The AGEMA measurements were used to calculate the fire radiant power (FRP), which is a measure of the radiant energy released by combustion (cf. Kaufman, Justice, et al., 1998 and Kaufman, Kleidman, et al., 1998). As demonstrated by Wooster et al. (2003) and Wooster et al. (2005), the FRP can be estimated directly from MIR radiance for fire temperatures between 650 and 1300 K.

Fig. 9 shows the spatial distribution of FRP over the Sharpsand Creek fire. We followed two approaches to simulate HyspIRI-scale temperatures. First, we aggregated the FRP over a 60 × 60-m (3600 m^2) region of interest centered over the hottest portion of the fire and converted the aggregated FRP, ~ 430 MW, into a temperature of ~ 1205 K through inversion of the Stefan–Boltzmann Law:

$$T = \sqrt[4]{FRP/(A\sigma)} \tag{2}$$

where A is the area of the aggregated region and σ is the Stefan–Boltzmann constant (5.67×10^{-8} W m^{-2} K^{-4}).

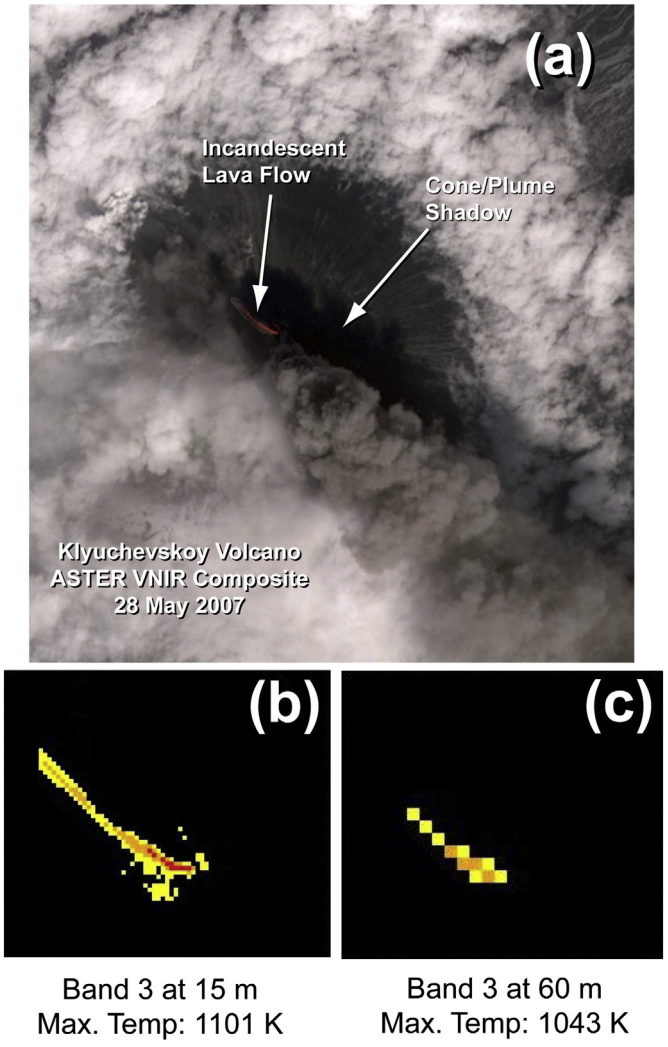

Fig. 10. Analysis of ASTER data acquired over Klyuchevskoy Volcano. (a) Color-composite of ASTER VNIR data showing incandescent lava flow in the shadow of an eruption plume. (b) Lava flow temperatures derived from Channel 3 (0.807 μm) radiance measurements. (c) Lava flow temperatures following aggregation of radiance data to 60-m spatial resolution of HyspIRI.

Please cite this article as: Realmuto, V.J., et al., Specifying the saturation temperature for the HyspIRI 4-μm channel, *Remote Sensing of Environment* (2015), http://dx.doi.org/10.1016/j.rse.2015.04.028

Our second approach was to aggregate the radiance measurements over the same region of interest and convert this aggregated radiance to brightness temperature. The aggregated radiance, ~7454 W m^{-2} sr^{-1} μm^{-1}, corresponds to a brightness temperature of ~1260 K. The FRP-based temperature estimate is within 5% of the radiance-based estimate, and this close agreement is a validation of the FRP estimation approach developed by Wooster et al. (2003) and Wooster et al. (2005).

4.3. ASTER surveys of Klyuchevskoy and Kilauea Volcanoes

Fig. 10 contains ASTER data acquired over Klyuchevskoy Volcano (Kamchatka Peninsula, Russia) on May 28, 2007, during an eruption episode that began on February 15, 2007, and ended on July 15, 2007. ASTER data acquired by the VNIR and SWIR subsystems feature spatial resolutions of 15 and 30 m, respectively, and radiance measurements in the VNIR and SWIR can be aggregated into HyspIRI-scale pixels.

The color-composite of VNIR data (Fig. 10a) reveals an incandescent lava flow within the shadow cast by an eruption plume. This lava flow was hot enough to saturate the SWIR measurements. Fortunately, the aforementioned shadow minimized the reflection of incident solar irradiance and thus facilitated the estimation of lava flow temperatures from the VNIR data. We applied an additional correction for reflected solar irradiance, following the procedure of Wooster and Kaneko (2001).

The twin panels below the VNIR color-composite are maps of lava flow temperatures derived from radiance measured in ASTER Channel 3 (centered at 0.807 μm). Fig. 10b shows the temperatures derived from the radiance at the native spatial resolution of 15 m, and Fig. 10c shows the temperatures derived from radiance aggregated to HyspIRI-scale (60 m) pixels. As shown in these temperature maps, the aggregation of radiance resulted in a decrease of ~60 K in the maximum observed temperature: 1101 vs. 1043 K.

Fig. 11 depicts ASTER data acquired over Kilauea Volcano, Hawaii, on November 25, 2007, during an outbreak of surface activity. These data

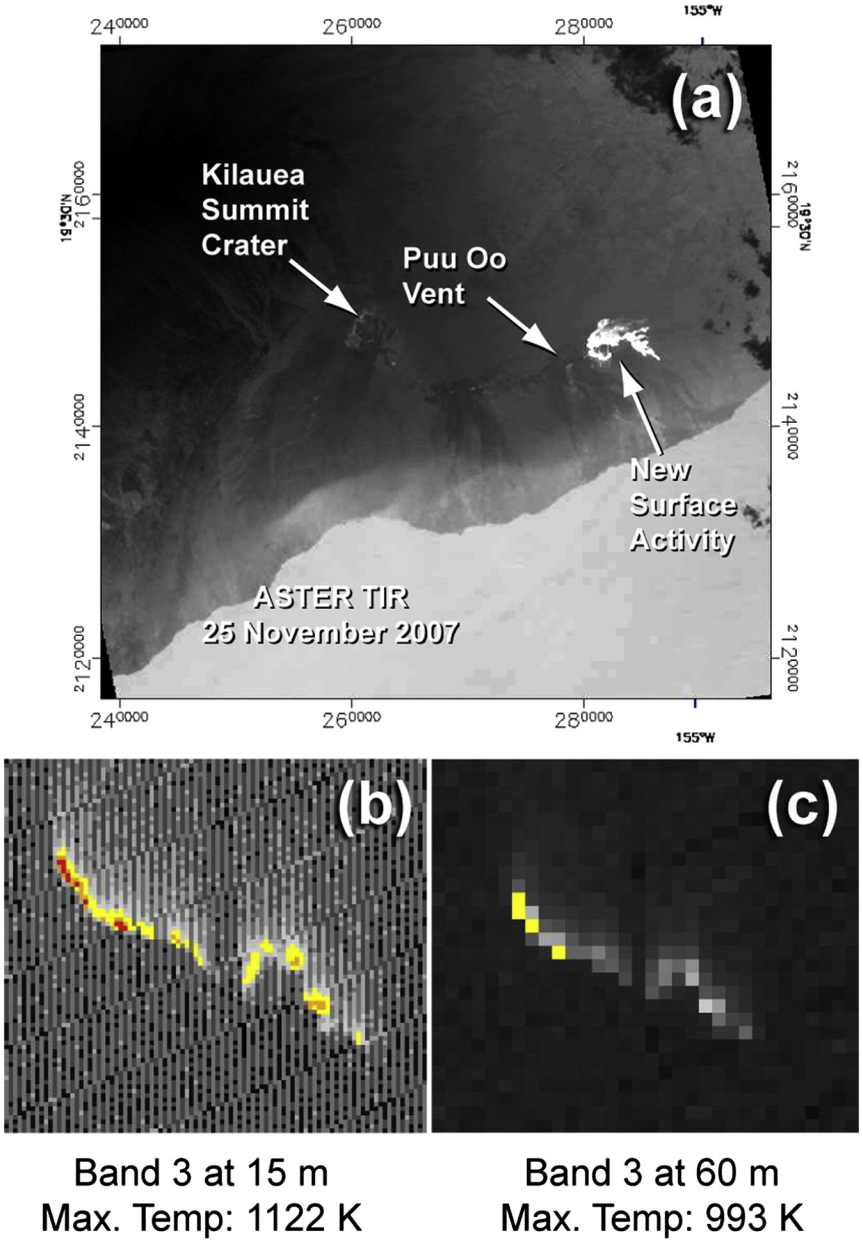

Fig. 11. Analysis of ASTER data acquired over Kilauea Volcano. (a) Night-time TIR data, showing active lava flow field. (b) Lava flow temperatures derived from Channel 3 (0.807 μm) radiance measurements. (c) Temperatures derived from radiance data aggregated to the 60-m spatial resolution of HyspIRI.

Please cite this article as: Realmuto, V.J., et al., Specifying the saturation temperature for the HyspIRI 4-μm channel, *Remote Sensing of Environment* (2015), http://dx.doi.org/10.1016/j.rse.2015.04.028

were acquired during a night-time overpass to eliminate the contributions of reflected solar irradiance to the temperature estimates. Fig. 11a shows the ASTER TIR scene, in which the active flow field is a prominent, albeit saturated, feature. The high temperatures of the active flows saturated the SWIR data as well. The twin panels below the TIR scene are temperature maps derived from Channel 3 radiance. Fig. 11b shows the temperatures derived from radiance at the native spatial resolution, and Fig. 11c shows the temperatures derived from Channel 3 radiance aggregated to HyspIRI-scale pixels. The aggregation resulted in a decrease of ~130 K in the maximum observed temperature: 1122 vs. 993 K. This large reduction in maximum temperature, relative to the reduction in the maximum temperature of the Klyuchevskoy flow (Fig. 10b vs. 10c), indicates that the hot spots at Kilauea were smaller (in terms of area) and more isolated than the hot spots at Klyuchevskoy.

4.4. Hyperion surveys of Nyamuragira and Eyjafjallajökull Volcanoes

Figs. 12 and 13 feature 4-μm temperature maps for Nyamuragira (DR-Congo) and Eyjafjallajökull (Iceland) Volcanoes, respectively, as simulated from hyperspectral V-SWIR radiance spectra measured with Hyperion. The Hyperion data were acquired at night to eliminate the contributions of reflected solar irradiance to the temperature estimates. At the time the Nyamuragira data were acquired, May 21, 2004, the activity at the volcano was near the end of an eruption episode that began on May 8, 2004 and ended sometime between May 25 and 31, 2004. The Eyjafjallajökull data were acquired on April 1, 2010, during an eruption that began on March 20, 2010. The data acquisition coincided with the opening of a new fissure on March 31, and the data depict lava fountains from both fissures.

For each pixel in the Hyperion data, we derived sub-pixel temperature components and corresponding area fractions through an application of the MMCM as described in Section 3.1. Due to the high spatial resolution of Hyperion (30 m), the resulting sub-pixel temperature components were too small to fill a HyspIRI pixel. To simulate HyspIRI observations at Nyamuragira and Eyjafjallajökull we calculated continuous (VIS through TIR) radiance spectra from the MMCM temperature distributions and then convolved these spectra with the spectral response of the HyspIRI MIR channel.

Figs. 12a and 13a are maps of the temperatures derived from this simulated radiance at a spatial resolution of 30 m. Figs. 12b and 13b are maps of temperatures derived from radiance aggregated to HyspIRI-scale pixels. The aggregation resulted in a reductions of approximately 150 and 350 K in the maximum temperatures for the Nyamuragira flow field (1100 vs. 950 K) and Eyjafjallajökull fissures (1100 vs. 750 K), respectively.

The bottom set of panels indicate the pixels that would be saturated with 4-μm saturation temperature settings of 800–1000 K (Fig. 12c, d, and e) in the case of Nyamuragira and 700–900 K in the case of Eyjafjallajökull (Fig. 13c, d, and e). We see that saturation temperature settings of 1000 and 900 K, respectively, would be required to prevent saturation of HyspIRI data acquired during Nyamuragira- and Eyjafjallajökull-class eruptions.

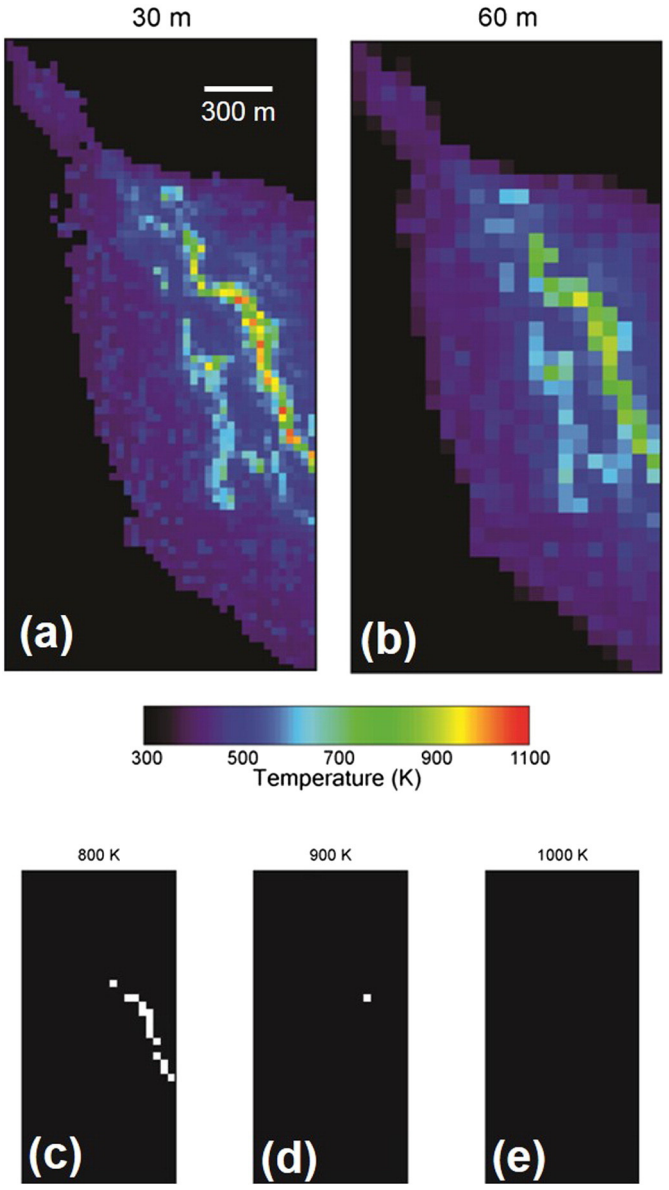

Fig. 12. Analysis of Hyperion data acquired over Nyamuragira Volcano on 21 May 2004. (a) Simulated 4-μm temperatures at the 30-m spatial resolution of Hyperion. (b) Simulated temperatures following aggregation of radiance data to the 60-m resolution of HyspIRI-TIR. (c–e) Locations of saturated pixels corresponding to proposed saturated temperatures of 800, 900, and 1000 K (527, 627, and 727 °C), respectively.

5. Conclusion

Table 3 summarizes the results of our literature review and case studies. The shaded entries were incorporated into our recommendation for the HyspIRI MIR saturation temperature. Based on these results we recommend a saturation temperature of 1200 K (927 °C) for the HyspIRI MIR channel. This threshold will result in NEΔT levels of 7.5–4.5 K for scene temperatures in the range 320–340 K, respectively (Fig. 2).

The threshold of 1200 K will prevent saturation for all of the temperatures considered in our study (Table 4) with the exception of the volcanic temperatures of 1325 and 1273 K reported by Harris et al. (1995) and Harris et al. (1997), respectively and those derived from the Sharpsand Fire test case (Section 4.2). In the case of the Sharpsand Fire, the higher of our simulated 60-m temperatures, 1260 K, is within 5% of the recommended saturation threshold. Similarly, the 1273 K temperature of Harris et al. (1997) is ~6% higher than the threshold. With regard to the other volcanic phenomena included in this study, we note that the proposed saturation threshold of 1200 K is higher than the Klyuchevskoy (Fig. 10b), Kilauea (Fig. 11b), Nyamuragira (Fig. 12a), or Eyjafjallajökull (Fig. 13a) temperatures estimated at the *native* spatial resolutions of ASTER or Hyperion.

However, the 1325 K temperature reported by Harris et al. (1995) is >10% higher than the recommend saturation threshold, and it is possible that HyspIRI will encounter wildfires with temperatures in excess of 1200 K over areas larger than 3600 m^2. An increase in the HyspIRI saturation threshold to 1400 K would accommodate these extreme events, with the consequence of increasing the NEΔT to ~7 K for scene temperatures ~340 K (Fig. 2). This increase in NEΔT, relative

Please cite this article as: Realmuto, V.J., et al., Specifying the saturation temperature for the HyspIRI 4-μm channel, *Remote Sensing of Environment* (2015), http://dx.doi.org/10.1016/j.rse.2015.04.028

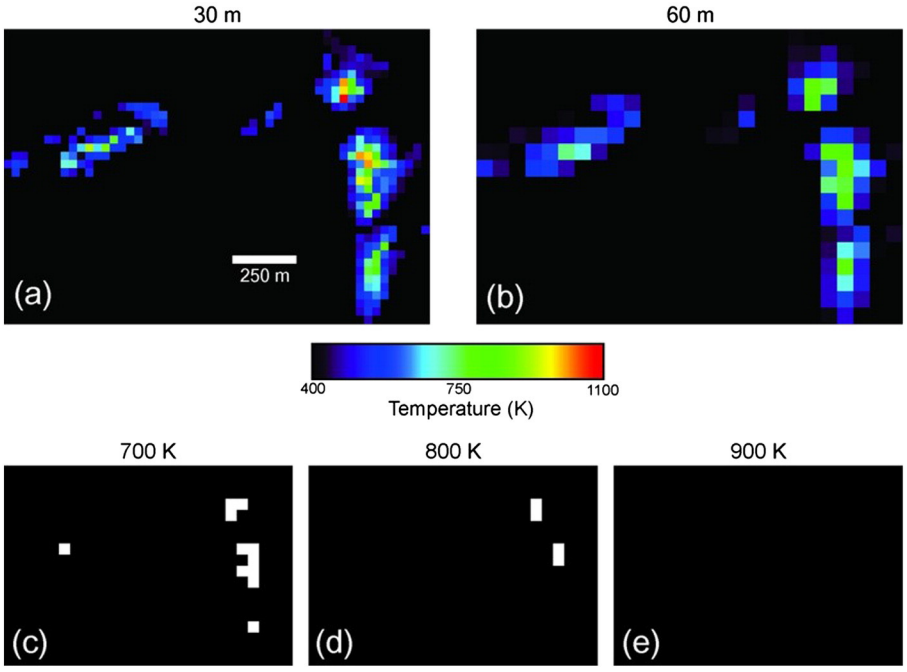

Fig. 13. Analysis of Hyperion data acquired over Eyjafallajökull Volcano on 1 April 2010. (a) Simulated 4-μm temperatures at 30-m spatial resolution of Hyperion. (b) Simulated temperatures following aggregation of radiance data to the 60-m resolution of HyspIRI-TIR. (c–e) Locations of saturated pixels corresponding to proposed saturation temperatures of 700, 800, and 900 K (427, 527, and 627 °C), respectively.

to our recommendation, represents a 56% loss in sensitivity to ambient background temperatures. Our study suggests that extreme temperature events (>1200 K) at the spatial resolution of HyspIRI are rare, and we judge that the loss in sensitivity to ambient temperatures will be more damaging to HyspIRI science investigations than the potential saturation during extreme temperature events.

The recommended NEΔT will be too high for precise measurements of land- and sea-surface temperatures with the HyspIRI MIR channel, but the TIR channels between 8 and 12 μm (Fig. 1) will be well-suited for studies of ambient surface temperatures. In addition, we note that HyspIRI data acquired over the oceans will be aggregated into 960-m pixels (representing 16 × 16 blocks of 60-m pixels). The corresponding 16-fold reduction in signal-independent noise will improve the NEΔT, and the precision of this aggregated MIR radiance data may fit the requirements of the sea-surface temperature community.

The trade-off between saturation temperature and sensitivity is particularly acute for the FRP technique, which depends on measurements of ambient background radiance. While the full impact of the proposed NEΔT on FRP has yet to be determined, the precision should be sufficient for most applications. For example, a smoldering fire at 700 K occupying 1% (36 m^2) of a HyspIRI pixel with a background temperature of 320 K would increase the MIR brightness temperature to ~380 K. Given an NEΔT of 7.5 K (at 320 K), the FRP of this modest fire could be calculated with an uncertainty of ±6%.

Acknowledgments

We thank the personnel of Airborne Sensor Facility, NASA/Ames Research Center, for access to the AMS image and calibration data. This paper is based, in part, on JPL Publication 11-2, *HyspIRI High-Temperature Saturation Study* (April, 2011). Both documents were prepared at the Jet Propulsion Laboratory, California Institute of Technology, under contract to the National Aeronautics and Space Administration. Copyright 2014, California Institute of Technology. Government participation acknowledged.

References

Ambrosia, V.G., & Hinkley, E. (2008). NASA science serving society: Improving capabilities for fire characterization to effect reduction in disaster losses. *Geoscience and remote sensing symposium, 2008. IGARSS 2008. IEEE International*, *Vol. 4*. (pp. IV-628–IV-631).

Andreae, M.O., & Merlet, D. (2001). Emission of trace gases and aerosols from biomass burning. *Global Biogeochemical Cycles*, *15*(4), 955–966.

Bradstock, R.A., & Auld, T.D. (1995). Soil temperatures during experimental brushfires in relation to fire intensity: Consequences for legume germination and fire management in south-eastern Australia. *Journal of Applied Ecology*, *32*(1), 76–84.

Briess, K., Jahn, H., Lorenz, E., Oertel, D., Skrbek, W., & Zhukov, B. (2003). Fire recognition potential of the Bi-spectral Infrared Detection (BIRD) satellite. *International Journal of Remote Sensing*, *24*(4), 865–872.

Brooks, M.L. (2002). Peak fire temperatures and effects on annual plants in the Mojave Desert. *Ecological Applications*, *12*(4), 1088–1102.

Crisp, J.A., & Baloga, S.M. (1990a). A model for lava flows with two thermal components. *Journal of Geophysical Research*, *95*(B2), 1255–1270.

Crisp, J.A., & Baloga, S.M. (1990b). A method for estimating eruption rates of planetary lava flows. *Icarus*, *85*, 512–515.

Csiszar, I.A., Morisette, J.T., & Giglio, L. (2006). Validation of active fire detection from moderate-resolution satellite sensors: The MODIS example in northern Eurasia. *IEEE Transactions on Geoscience and Remote Sensing*, *44*(7), 1757–1764. http://dx.doi.org/10.1109/TGRS.2006.875941.

Csiszar, I., & Sullivan, J. (2002). Recalculated pre-launch saturation temperatures of the AVHRR 3.7 μm sensors on board the TIROS-N to NOAA-14 satellites. *International Journal of Remote Sensing*, *23*(24), 5271–5276.

Csiszar, I.A., et al. (2014). Active fires from the Suomi NPP Visible Infrared Imaging Radiometer Suite: Product status and first evaluation results. *Journal of Geophysical Research, Atmospheres*, *119*. http://dx.doi.org/10.1002/2013JD020453.

DeBano, L.F. (2000). The role of fire and soil heating on water repellency in wildland environments: A review. *Journal of Hydrology*, *231–232*, 195–206.

Dennison, P.E., Charoensiri, K., Roberts, D.A., Peterson, S.H., & Green, R.O. (2006). Wildfire temperature and land cover modeling using hyperspectral data. *Remote Sensing of Environment*, *100*(2), 212–222.

Dennison, P.E., & Matheson, D.S. (2011). Comparison of fire temperature and fractional area modeled from SWIR, MIR, and TIR multispectral and SWIR hyperspectral airborne data. *Remote Sensing of Environment*, *115*(3), 876–886. http://dx.doi.org/10.1016/j.rse.2010.11.015.

Dozier, J. (1981). A method for satellite identification of surface temperature fields of subpixel resolution. *Remote Sensing of Environment*, *11*, 221–229.

Drewa, P.B., Platt, W.J., & Moser, E.B. (2002). Fire effects on resprouting of shrubs in headwaters of southeastern longleaf pine savannas. *Ecology*, *83*(3), 757–767.

Eckmann, T.C., Roberts, D.A., & Still, C.J. (2008). Using multiple endmember spectral mixture analysis to retrieve subpixel fire properties from MODIS. *Remote Sensing of Environment*, *112*, 3773–3783.

Eckmann, T.C., Roberts, D.A., & Still, C.J. (2009). Estimating subpixel fire sizes and temperatures from ASTER using multiple endmember spectral analysis. *International Journal of Remote Sensing, 30*(22), 5851–5864.

Elvidge, C.D., Zhizhin, M., Hsu, F.C., & Baugh, K.E. (2013). VIIRS nightfire: Satellite pyrometry at night. *Remote Sensing, 5*, 4423–4449.

Gao, B. -C., Xiong, X., Li, R. -R., & Wang, R. -R. (2007). Evaluation of the Moderate Resolution Imaging Spectrometer special 3.95-μm fire channel and implications on fire channel selections for future satellite instruments. *Journal of Applied Remote Sensing, 1*, 013516. http://dx.doi.org/10.1117/1.2757715.

Giglio, L., Csiszar, I., Restas, A., Morisette, J.T., Schroeder, W., Morton, D., et al. (2008). Active fire detection and characterization with the advanced spaceborne thermal emission and reflection radiometer (ASTER). *Remote Sensing of Environment*, *112*, 3055–3063. http://dx.doi.org/10.1016/j.rse.2008.03.003.

Giglio, L., Descloitres, J., Justice, C.O., & Kaufman, Y.J. (2003). An enhanced contextual fire detection algorithm for MODIS. *Remote Sensing of Environment*, *87*, 273–282. http://dx.doi.org/10.1016/S0034-4257(03)00184-6.

Giglio, L., & Kendall, J.D. (2001). Application of the Dozier retrieval to wildfire characterization — A sensitivity analysis. *Remote Sensing of Environment*, *77*, 34–49.

Giglio, L., Kendall, J.D., & Justice, C.O. (1999). Evaluation of global fire detection algorithms using simulated AVHRR infrared data. *International Journal of Remote Sensing, 20*(10), 1947–1985.

Giglio, L., Kendall, J.D., & Mack, R. (2003). A multi-year active fire dataset for the tropics derived from the TRMM VIRS. *International Journal of Remote Sensing*, *24*(22), 4505–4525. http://dx.doi.org/10.1080/0143116031000070283.

Giglio, L., Kendall, J.D., & Tucker, C.J. (2000). Remote sensing of fires with the TRMM VIRS. *International Journal of Remote Sensing, 21*(1), 203–207.

Glaze, L., Francis, P.W., & Rothery, D.A. (1989). Measuring thermal budgets of active volcanoes by satellite remote sensing. *Nature*, *338*(6211), 144–146.

Harris, A.J.L., & Baloga, S.M. (2009). Lava discharge rates from satellite-measured heat flux. *Geophysical Research Letters*, *36*. http://dx.doi.org/10.1029/2009GL039717 (L19302).

Harris, A.J.L., Blake, S., Rothery, D.A., & Stevens, N.F. (1997). A chronology of the 1991 to 1993 Etna eruption using advanced very high resolution radiometer data: Implications for real-time thermal volcano monitoring. *Journal of Geophysical Research*, *102*, 7985–8003.

Harris, A.J.L., Dehn, J., & Calvari, S. (2007). Lava effusion rate definition and measurement: A review. *Bulletin of Volcanology*, *70*, 1–22.

Harris, A.J.L., Flynn, L.P., Rothery, D.A., Oppenheimer, C., & Sherman, S.B. (1999). Mass flux measurements at active lava lakes. *Journal of Geophysical Research*, *104*(B4), 7117–7136.

Harris, A.J.L., Pilger, E., Flynn, L.P., Garbeil, H., Mouginis-Mark, P.J., Kauahikaua, J., et al. (2001). Automated, high temporal resolution, thermal analysis of Kilauea volcano, Hawai'i, using GOES satellite data. *International Journal of Remote Sensing*, *22*, 945–967.

Harris, A.J.L., & Thornber, C.R. (1999). Complex effusive events at Kilauea as documented by the GOES satellite and remote video cameras. *Bulletin of Volcanology*, *61*, 382–395.

Harris, A.J.L., Vaughan, R.A., & Rothery, D.A. (1995). Volcano detection and monitoring using AVHRR data: The Krafla eruption, 1984. *International Journal of Remote Sensing, 16*(6), 1001–1020.

Justice, C.O., et al. (2002). The MODIS fire products. *Remote Sensing of Environment*, *83*, 244–262.

Kaneko, T., Wooster, M.J., & Nakada, S. (2002). Exogeneous and endogenous growth of the Unzen lava dome examined by satellite infrared image analysis. *Journal of Volcanology and Geothermal Research*, *116*, 151–160.

Kaufman, Y.J., Ichoku, C., Giglio, L., Korontzi, S., Chu, D.A., Hao, W.M., et al. (2003). Fire and smoke observed from Earth Observing System MODIS instrument — Products, validation, and operational use. *International Journal of Remote Sensing, 24*(8), 1765–1781.

Kaufman, Y.J., Justice, Flynn, L.P., Kendall, J.D., Prins, E.M., Giglio, L., et al. (1998). Potential global fire monitoring from EOS-MODIS. *Journal of Geophysical Research*, *103*(D24), 32,215–32,238.

Kaufman, Y.J., Kleidman, R.G., & King, M.D. (1998). SCAR-B fires in the tropics: Properties and remote sensing from EOS-MODIS. *Journal of Geophysical Research*, *103*(D24), 31,955–31,968.

Langaas, S. (1993). A parameterised bispectral model for savanna fire detection using AVHRR night images. *International Journal of Remote Sensing, 14*(12), 2245–2262.

Lombardo, V., & Buongiornio, M.F. (2006). Lava flow thermal analysis using three infrared bands of remote sensing imagery: A case study from the Mount Etna 2001 eruption. *Remote Sensing of Environment*, *101*, 141–149.

Lombardo, V., Buongiorno, M.F., & Amici, S. (2006). Characterization of volcanic thermal anomalies by means of sub-pixel temperature distribution analysis. *Bulletin of Volcanology*, *68*, 641–651.

Lombardo, V., Harris, A.J.L., Calvari, S., & Buongiornio, M.F. (2009). Spatial variation in lava flow field thermal structure and effusion rate derived from very high spatial resolution hyperspectral (MIVIS) data. *Journal of Geophysical Research*, *114*. http://dx.doi.org/10.1029/2008JB005648 (B02208).

Lombardo, V., Merucci, L., & Buongiorno, M.F. (2006). Wavelength influence in sub-pixel temperature retrieval using the dual-band technique. *Annals of Geophysics*, *49*(1), 227–234.

Matheson, D.S., & Dennison, P.E. (2012). Evaluating the effects of spatial resolution on hyperspectral fire detection and temperature retrieval. *Remote Sensing of Environment*, *124*, 780–792.

Matson, M., & Dozier, J. (1981). Identification of subresolution high temperature sources using a thermal IR sensor. *Photogrammetric Engineering and Remote Sensing*, *47*(9), 1311–1318.

National Research Council (2007). *Earth science and applications from space: National imperatives for the next decade and beyond, 11820.* Washington D.C.: National Academies Press (456 pp.).

Odion, D.C., & Davis, F.W. (2000). Fire, soil heating, and the formation of vegetation patterns in chaparral. *Ecological Monographs*, *70*(1), 149–169.

Oertel, D., Zhulov, B., Thamm, H. -P., Roehrig, J., & Orthmann, B. (2004). Space-borne high resolution fire remote sensing in Benin, West Africa. *International Journal of Remote Sensing, 25*(11), 2209–2216.

Oppenheimer, C., Francis, P.W., Rothery, D.A., & Carlton, R.W.T. (1993). Infrared image analysis of volcanic thermal features: Lascar Volcano, Chile, 1984–1992. *Journal of Geophysical Research*, *98*(B3), 4269–4286.

Oppenheimer, C., Rothery, D.A., Pieri, D.C., Abrams, M.J., & Carrere, V. (1993). Analysis of Airborne Visible/Infrared Imaging Spectrometer data of volcanic hot spots. *International Journal of Remote Sensing, 14*(16), 2919–2934.

Pereira, G., et al. (2009). Estimating trace gas and aerosol emissions over South America: Relationship between fire radiative energy released and aerosol optical depth observations. *Atmospheric Environment*, *43*, 6388–6391. http://dx.doi.org/10.1016/j.atmosenv.2009.09.013.

Pieri, D.C., & Baloga, S.M. (1986). Eruption rate, area, and length relationships for some Hawaiian lava flows. *Journal of Volcanology and Geothermal Research*, *30*, 29–45.

Prakash, A., & Gupta, R.P. (1999). Surface fires in Jharia coalfield, India — Their distribution and estimation of area and temperature from TM data. *International Journal of Remote Sensing, 20*(10), 1935–1946.

Riggan, P.J., Brass, J.A., & Lockwood, R.N. (1993). Assessing fire emissions from tropical savanna and forest of central Brazil. *Photogrammetric Engineering and Remote Sensing, 59*(6), 1009–1015.

Riggan, P.J., Tissell, R.G., Lockwood, R.N., Brass, J.A., Pereira, J.A.R., Miranda, H.S., et al. (2004). Remote measurement of energy and carbon flux from wildfires in Brazil. *Ecological Applications, 14*(3), 855–872.

Roberts, D.A., et al. (1998). Mapping chaparral in the Santa Monica Mountains using multiple endmember spectral mixture models. *Remote Sensing of Environment*, *65*, 267–279.

Roberts, G., et al. (2005). Retrieval of biomass combustion rates and totals from fire radiative power observations: Application to southern Africa using geostationary SEVIRI imagery. *Journal of Geophysical Research*, *110*. http://dx.doi.org/10.1029/2005JD006018 (D21111).

Rose, S., & Ramsey, M. (2009). The 2005 eruption of Kliuchevskoi volcano: Chronology and processes derived from ASTER spaceborne and field-based data. *Journal of Volcanology and Geothermal Research*, *184*, 367–380. http://dx.doi.org/10.1016/j.volgeores.2009.05.001.

Rothery, D.A., Coltelli, M., Pirie, D., Wooster, M.J., & Wright, R. (2001). Documenting surface magmatic activity at Mount Etna using ATSR remote sensing. *Bulletin of Volcanology*, *63*, 387–397.

Rothery, D.A., Francis, P.W., & Wood, C.A. (1988). Volcano monitoring using short wavelength infrared data from satellites. *Journal of Geophysical Research*, *93*(B7), 7993–8008.

Rowland, S.K., Garbeil, H., & Harris, A.J.S. (2005). Lengths and hazards from channel-fed lava flows on Mauna Loa, Hawaii, determined from thermal and downslope modeling with FLOWGO. *Bulletin of Volcanology*, *67*, 634–647.

Schroeder, W., Oliva, P., Giglio, L., & Csiszar, I.A. (2014). The new VIIRS 375 m active fire detection product: Algorithm description and initial assessment. *Remote Sensing of Environment*, *143*, 85–96. http://dx.doi.org/10.1016/j.rse.2013.12.008.

Siegert, F., et al. (2004). Peat fires detected by the BIRD satellite. *International Journal of Remote Sensing, 25*(16), 3221–3230.

Smith, D.R., et al. (2010). Soil surface CO_2 flux increases with successional time in a fire scar chronosequence of Canadian boreal jack pine forest. *Biogeosciences*, *7*, 1375–1381. http://dx.doi.org/10.5194/bg-7-1375-2010.

Vaughan, R.G., Kervyn, M., Realmuto, V., Abrams, M., & Hook, S.J. (2008). Satellite measurements of recent volcanic activity at Oldoinyo Lengai, Tanzania. *Journal of Volcanology and Geothermal Research*, *173*, 196–206.

Vaughan, R.G., Keszthelyi, L.P., Davies, A.G., Schneider, D.J., Jaworowski, C., & Heasler, H. (2010). Exploring the limits of identifying sub-pixel thermal features using ASTER TIR data. *Journal of Volcanology and Geothermal Research*, *189*, 225–237.

Wooster, M.J., & Kaneko, T. (2001). Testing the accuracy of solar-reflected radiation corrections applied during satellite shortwave infrared thermal analysis of active volcanoes. *Journal of Geophysical Research*, *106*(B7), 13,381–13,393.

Wooster, M.J., Kaneko, T., Nakada, S., & Shimizu, H. (2000). Discrimination of lava dome activity styles using satellite-derived thermal structures. *Journal of Volcanology and Geothermal Research*, *102*, 97–118.

Wooster, M.J., Roberts, G., Perry, G.L.W., & Kaufman, Y.J. (2005). Retrieval of biomass combustion rates and totals from fire radiant power observations: FRP derivation and calibration relationship between biomass consumption and fire radiative energy release. *Journal of Geophysical Research*, *110*. http://dx.doi.org/10.1029/2005JD006318 (D24311).

Wooster, M.J., & Rothery, D.A. (1997). Thermal monitoring of Lascar Volcano, Chile, using infrared data from the along-track scanning radiometer: A 1992–1995 time series. *Bulletin of Volcanology*, *58*, 566–579.

Wooster, M.J., Zhukov, B., & Oertel, D. (2003). Fire radiative energy for quantitative study of biomass burning: Derivation from the BIRD experimental satellite and comparison to MODIS fire products. *Remote Sensing of Environment*, *86*, 83–107.

Wright, R., & Flynn, L.P. (2003). On the retrieval of lava-flow surface temperatures from infrared satellite data. *Geology*, *31*, 893–896.

Wright, R., Flynn, L., Garbeil, H., Harris, A., & Pilger, E. (2002). Automated volcanic eruption detection using MODIS. *Remote Sensing of Environment*, *82*, 135–155.

Wright, R., Flynn, L.P., Garbeil, H., Harris, A.J.L., & Pilger, E. (2004). MODVOLC: Near-real-time thermal monitoring of global volcanism. *Journal of Volcanology and Geothermal Research*, *135*, 29–49.

Please cite this article as: Realmuto, V.J., et al., Specifying the saturation temperature for the HyspIRI 4-μm channel, *Remote Sensing of Environment* (2015), http://dx.doi.org/10.1016/j.rse.2015.04.028

Wright, R., Flynn, L.P., & Harris, A.J.L. (2001). Evolution of lava flow-fields at Mount Etna, 27–28 October 1999, observed by Landsat ETM+. *Bulletin of Volcanology, 63*, 1–7.

Wright, R., Garbeil, H., & Davies, A.G. (2010). Cooling rate of some active lavas determined using an orbital imaging spectrometer. *Journal of Geophysical Research*, *115*. http://dx.doi.org/10.1029/2009JB006536 (B06205).

Wright, R., Garbeil, H., & Harris, A.J.L. (2008). Using infrared satellite data to drive a thermo-rheological/stochastic lava flow emplacement model: A method for near-real-time volcanic hazard assessment. *Geophysical Research Letters*, *35*. http://dx.doi.org/10.1029/2008GL035228 (L19307).

Xu, W., Wooster, M.J., Roberts, G., & Freeborn, P. (2010). New GOES imager algorithms for cloud and active fire detection and fire radiative power assessment across North, South, and Central America. *Remote Sensing of Environment, 114*, 1876–1895.

Zhukov, B., et al. (2003). BIRD detection and analysis of high-temperature events: First results. *Proceedings of SPIE 4886, remote sensing for environmental monitoring, GIS applications, and geology* (pp. 160–171).

Zhukov, B., et al. (2005). Detection and analysis of high-temperature events in the BIRD mission. *Acta Astronautica, 56*, 65–71.

Zhukov, B., et al. (2006). Spaceborne detection and characterization of fires during the bi-spectral infrared detection (BIRD) experimental small satellite mission (2001–2004). *Remote Sensing of Environment, 100*, 29–51.

Please cite this article as: Realmuto, V.J., et al., Specifying the saturation temperature for the HyspIRI 4-μm channel, *Remote Sensing of Environment* (2015), http://dx.doi.org/10.1016/j.rse.2015.04.028